

Finding Near-Surface Ice on Mars From Radar Images

Nathan Chan

Advisor: Professor Thomas Lee

Special thanks to Sam Wagner

Department of Statistics

University of California, Davis

September 30, 2020

njchan@ucdavis.edu

<https://github.com/nathanjchan/ice-on-mars>

Abstract

Utilizing the near-surface ice on Mars just centimeters under the Martial soil is essential to human exploration of the planet. SHARAD, a ground-penetrating radar in orbit around Mars, is too low resolution to differentiate between the soil and ice. Radar reflections from these two indistinguishable subsurface layers create speckle-like interference, which is the background noise in processed SHARAD radar images. I quantify this speckle-like interference in each radar image using texture features from gray-level co-occurrence matrices. I label each image with whether or not near-surface ice exists at the location of the image based on an ice depth map of Mars from previous research. I find that machine learning with random forest predicts the presence of near-surface ice from the radar image texture with 87% accuracy, suggesting it is possible to measure speckle-like interference and use it to find near-surface ice on Mars and beyond.

1 Introduction

1.1 Ice on Mars

To ensure life and consciousness extend beyond the inevitable death of Earth, humanity will become a space-faring civilization and colonize the galaxy and universe, starting with Mars, the closest and most habitable planet. Mars is the ideal candidate for human colonization because it contains useful minerals in the ground, useful gases in the atmosphere, and water, in the form of ice, underground all over the planet (Barlow, 2008). Much of the subsurface ice is *near-surface ice*: ice all over Mars just centimeters under the Martian sand-like soil (Boynton et al., 2002). Identifying the specific locations of near-surface ice on Mars is necessary to help determine where to land so explorers can make the most use of the planet's resources (Beaty et al., 2016).

Ground-penetrating radar is one method of identifying subsurface ice on Mars. MARSIS (Mars Advanced Radar for Subsurface and Ionosphere Sounding), on the Mars Express spacecraft (Picardi et al., 2005), and SHARAD (Mars SHAllow RADar sounder), on the Mars Reconnaissance Orbiter spacecraft (Seu et al., 2007), are the two ground-penetrating radars currently orbiting Mars. Researchers used MARSIS to study the properties of visible ice at the north and south poles (Picardi et al., 2005; Plaut et al., 2006) and even discovered liquid water in an underground lake under a glacier (Orosei et al., 2018), but there are no plans to send explorers up to these high latitudes (Piqueux et al., 2019). Researchers also used SHARAD to find subsurface ice under lobate debris aprons: geological structures in the northern mid-latitudes of Mars that are hundreds of meters thick (Plaut et al., 2009). The conditions there are optimal for human landings, but extracting the ice may be difficult (Piqueux et al., 2019).

Asteroid impacts (Dundas et al., 2014) and the Phoenix Mars lander (Mellon et al., 2009)

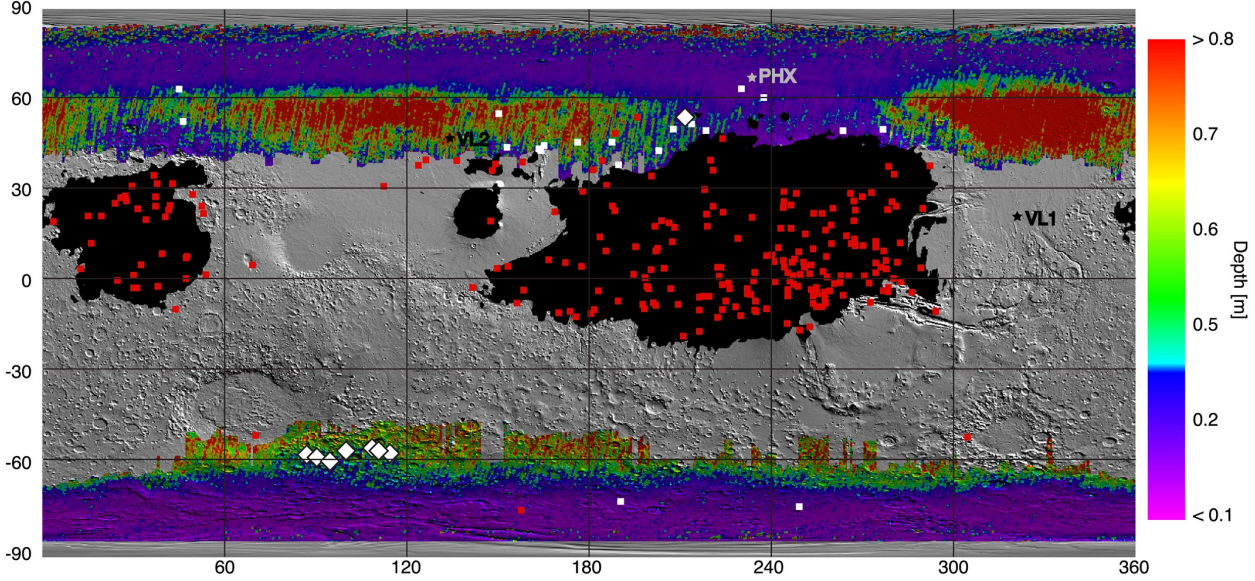


Figure 1: From Piqueux et al. (2019): “Depth to the top of the water ice table d derived from MCS data. Background is a MOLA shaded relief. Low thermal inertia regions unsuitable for landing are masked out. PHX, VL1, and VL2 indicate the landing site locations for Phoenix, Viking Lander 1, and Viking Lander 2. White squares indicate fresh ice-exposing impact craters (red squares mean no ice identified). White diamonds indicate exposed water ice along cliff scarps.”

confirmed the existence of near-surface ice on Mars. Unfortunately, the MARSIS and SHARAD radars are too low resolution to directly observe the near-surface ice (Putzig et al., 2014). Due to the radar’s frequency, SHARAD has a 15-meter vertical depth resolution (Seu et al., 2007) and MARSIS has a 150-meter depth resolution (Picardi et al., 2005), meaning each radar can only detect subsurface layers that are separated by more than 15 or 150 meters. The radars cannot differentiate the soil surface and the ice that is only a few centimeters underneath the surface.

Researchers have developed other techniques to map the near-surface ice. In one method, Piqueux et al. (2019) used the seasonal temperature trends of the Martian surface to model the location and depth of near-surface ice all over Mars, made possible by understanding how the ice interacts with the surface temperature.

1.2 Ground-Penetrating Radar

The SHARAD ground-penetrating radar works by transmitting electromagnetic waves towards the surface, where the waves either continue through the surface, scatter in many directions, or reflect back at the radar receiver for collection (Seu et al., 2007). Researchers use the signals to create a radar image, or a radargram, a two-dimensional image slice of the subsurface (Campbell & Phillips, 2014).

The electromagnetic wave reflects back towards the radar receiver when there is a change in permittivity (a material's electric polarizability) or permeability (a material's resistance to the formation of a magnetic field) due to different ground materials, like soil or ice. (The reflected electromagnetic wave is the reflection, which is simply the wave bouncing off the surface in the opposite direction.) The separate layers of soil and ice will create two main reflections. Note that there are also an infinite number of exponentially decaying minor reflections from multipath propagation.

Speckle is the noise that occurs when many reflections within the same radar resolution interfere with each other and is the background noise that appears in processed radar images. The soil and ice reflections are within SHARAD's 15-meter resolution, so they will interfere with each other. These two main reflections will combine into a single reflection that SHARAD will measure, which causes interference.

SHARAD measures the frequency-domain response of the reflection, meaning it observes the reflection's frequency instead of how the reflection changes over time. For the frequency-domain response, SHARAD is interested in the magnitude and phase of the reflection, which are two ways to measure an electromagnetic wave. The interference from multiple reflections manifests itself as

changes in the frequency-domain response of the reflections.

1.3 Hypothesis

The near-surface ice may be causing *speckle-like interference* in the radar data, which are present in processed radar images as different textures. Texture features can quantify the radar image's texture, and machine learning can find whether near-surface ice exists at the location of an image, because the background noise (the texture) is different when there is ice.

2 Methods

2.1 Dataset

With SHARAD data from December 6, 2006, to November 19, 2019, the United States SHARAD team has created 24,038 SHARAD radar images, which they store on the Geosciences Node of the NASA Planetary Data System (Campbell & Phillips, 2014). I programmatically detected 388 images that have large vertical gaps from processing errors, leaving 23,650 images in the dataset.

Each radar image contains the start and end coordinates in longitude and latitude. I calculated the center coordinate of the radar image and used the ice depth map from Piqueux et al. (2019) to find whether or not there is near-surface ice in that image, under a strong assumption that the ice depth model is accurate. According to the model, 14,283 radar images have no near-surface ice at the center (so, either no ice or very deep ice), and 9,367 radar images have near-surface ice at the center.

All the images have a height of 3,600 pixels, while widths vary from 139 to 21,225 pixels.

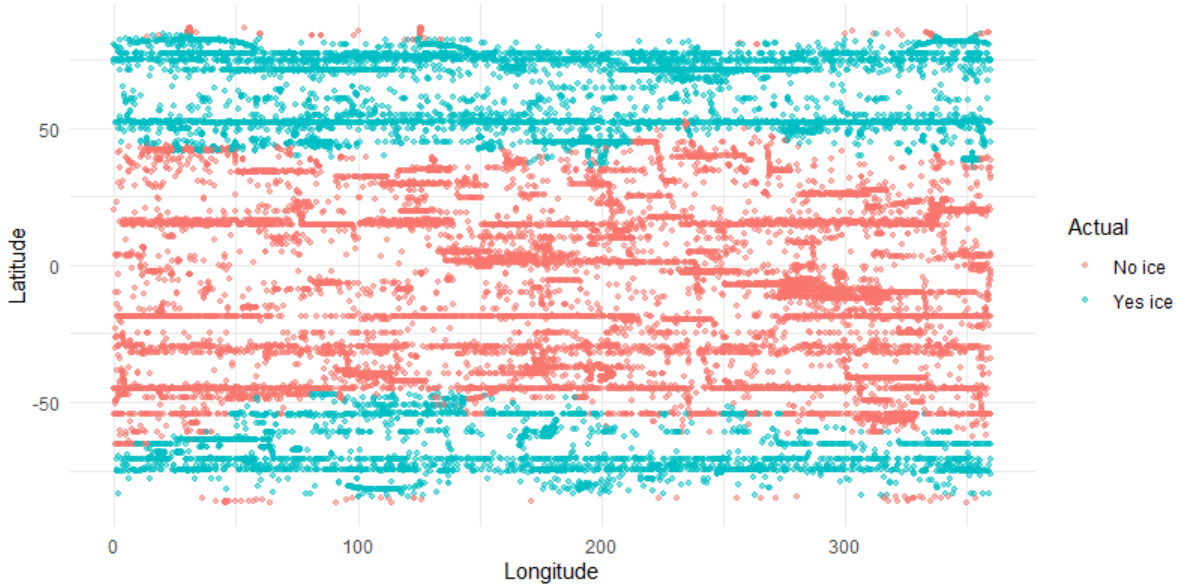


Figure 2: Locations of radar images on Mars with and without near-surface ice based on the center coordinate of the image and the output of the model from Piqueux et al. (2019).

I cropped each radar image to 64 pixels because the length of 64 pixels corresponds to 29.75 kilometers on Mars’s surface that the radar travels, which is the same resolution of the ice depth model from Piqueux et al. (2019).

2.2 Image Features

Performing machine learning on images requires numbers, called features, to mathematically describe the image. Researchers have developed image features for applications like searching and retrieving specific images from databases or classifying images into groups (Zhang et al., 2012).

In this image classification study, the classification label is yes or no for the presence of near-surface ice at the center location of the radar image. The purpose of image features is to measure the speckle-like interference in the radar image.

Computers store images as a matrix, where each matrix entry is a scalar or vector that represents the color of each pixel. Calculating features is simply creating useful combinations of these matrix

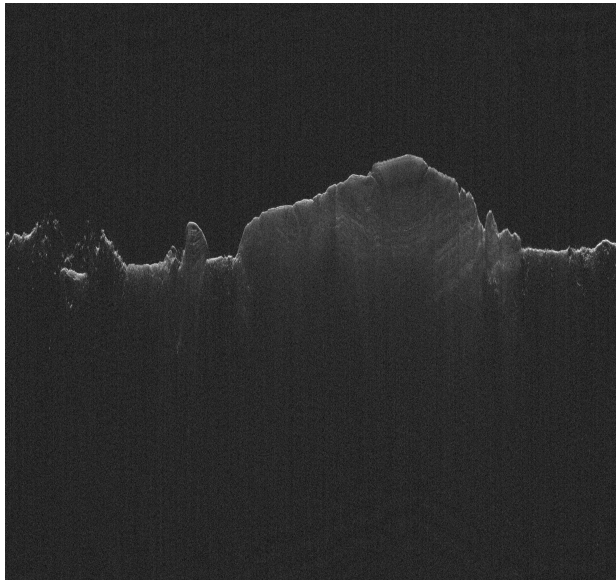


Figure 3: Radar image, or radargram, from SHARAD ground-penetrating radar with a width of 3,816 pixels. Left side at coordinate {longitude: 106.836, latitude: -71.934}, right side at coordinate {longitude: 305.462, latitude: -77.872}.



Figure 4: Radar image cropped to a width of 64 pixels at coordinates {longitude: 26.149, latitude: -74.903}. Based on the model from Piqueux et al. (2019), there is ice 0.0429 meters under the surface.

entries. For a radar image, each matrix entry is a single integer scalar from 0 to 255, representing the color of the pixel. We can interpret these colors as varying shades of gray, or gray-levels.

A *descriptor* is a general idea that describes an image, while a *feature* is a single number that describes an image. I use *color* and *gray-level* interchangeably, since all radar images are black-and-white and made up of gray-levels. For radar, the color or gray-level can also be called *intensity*.

2.3 Color Distribution

The distribution of color is a simple image descriptor. One way to describe the distribution of color is to calculate the distribution's moments: the mean, standard deviation, skewness, and kurtosis of all the pixel values (Long et al., 2003). These moments are 4 features. The color histogram is another way to describe the distribution of color, where we group pixel values into bins and count them (Swain & Ballard, 1991). I divided the 256 colors in the radar image into 32 bins of equal size, with each bin being the percentage of total pixels in the image belonging to the corresponding color bin, creating 32 image features.

With the 4 moment features and 32 bin features, we have $4 + 32 = 36$ features for each radar image. The machine learning algorithm doesn't receive the image; rather, it receives the vector of 36 values. These color features are useful for applications like image retrieval, but they are not necessarily useful for identifying small nuances in the radar images, so we turn to more sophisticated image features.

2.4 Gray-Level Co-Occurrence Matrix

Compared to color features, which calculate features from individual pixel values, texture features calculate features from groups of pixels (Zhang et al., 2012), providing a much deeper understanding of the image. Humans have an intuitive understanding of image texture, and there are multiple ways to describe it to a computer. An example application of texture features is the classification of ground terrain from aerial photographs (Haralick et al., 1973).

I present a new application of texture features. From the SHARAD ground-penetrating radar image, I use texture features to quantify the speckle-like interference in the radar image's backscatter returns. I then use machine learning to differentiate the textures into two groups: whether or not there is near-surface ice at the location of the radar image.

The gray-level co-occurrence matrix (GLCM) is a texture descriptor that describes the relationship between pixels based on their position compared to pixels of the same color (Haralick et al., 1973). From a sliding window around an image, one derives a GLCM for each window and calculates multiple texture descriptors from that GLCM, like homogeneity, contrast, and dissimilarity (Zvoleff, 2020). Contrast, for example, ends up being a set of numbers the size of the number of GLCMs. Like the color distribution, to turn the descriptors into useful features, I took the 4 moments of the distribution of the descriptors, a method that yields surprising results.

I used the R package *glcm* from Zvoleff (2020) to calculate the GLCM descriptors. I will explain the calculations in the context of this study here.

We start with a radar image. To shorten computation time, we quantize the image to $K = 32$ colors, meaning we group pixels into $K = 32$ groups, decreasing the numbers of colors from 256 to 32. Since pixel values range from 0 to 255, any pixel value ≥ 0 and < 8 becomes 1, any pixel

The figure consists of three 4x4 grids of integers.
 Grid (a) shows a 3x3 window centered at (2,2) with a red border, and a 3x3 window centered at (1,1) with a blue border.
 Grid (b) shows a 3x3 window centered at (2,2) with a red border, and a 3x3 window centered at (1,1) with a blue border.
 Grid (c) shows a 3x3 window centered at (2,2) with a red border, and a 3x3 window centered at (1,1) with a blue border.

3	5	3	4
3	6	4	3
2	4	3	4
1	2	2	3

3	5	3	4
3	6	4	3
2	4	3	4
1	2	2	3

3	5	3	4
3	6	4	3
2	4	3	4
1	2	2	3

(a) With a 3x3 window and pixel neighbors at $\theta = -45^\circ$, a 4x4 image will lead to $M = 1$ possible window and $M = 1$ possible GLCM.

(b) With a 3x3 window and pixel neighbors at $\theta = -90^\circ$, a 4x4 image will lead to $M = 2$ possible windows and $M = 2$ possible GLCMs.

(c) For a 3x3 image, we cannot use a 3x3 window because neighbors for some pixels do not exist.

Figure 5: How angle of pixel neighbors and window size affects number of possible windows.

value ≥ 8 and < 16 becomes 2, and so on, up to and including 32. The reason we choose values 1 to 32 instead of 0 to 31 is that later calculations require indexing to start from 1.

Then, we choose an angle θ to decide which pixel will be another pixel's designated neighbor.

We'll use a $\theta = -45^\circ$ angle. Any given pixel's neighbor will be the pixel to its southeast: one pixel down and one pixel right.

Next, we choose an arbitrary sliding window size $W \times W$. Let's say $W = 3$, so we have a 3x3 sliding window. The two conditions for W are that 1) W must be odd, so there is a center of the window where we can represent the texture of the window with a single value, and 2) W must be small enough such that every pixel in the window has a designated neighbor for that image. In our case, with $\theta = -45^\circ$, pixels on the bottom edge and right edge of the window will have neighbors outside the window. For a 3x3 image, we cannot use a 3x3 window because neighbors for some pixels do not exist.

Finally, we obtain M GLCMs from M possible windows (where every pixel in the window has a neighbor). In our case, with a 3x3 window and pixel neighbors at a $\theta = -45^\circ$ angle, a 4x4 image will lead to $M = 1$ possible window and $M = 1$ possible GLCM. If we chose pixel neighbors at a $\theta = -90^\circ$ angle, a 4x4 image will lead to $M = 2$ possible windows and $M = 2$ possible GLCMs.

The GLCM is a $K \times K$ matrix based on the number of colors K . Since we have $K = 32$ colors, the GLCM will be a 32x32 matrix, with rows indexed by $i = 1, 2, \dots, 32$ and columns indexed by $j = 1, 2, \dots, 32$. For a 3x3 sliding window, there are $P = 9$ pixel value pairs (x, y) , where $P = W^2$ is the number of pixel value pairs (and the number of pixels in the sliding window), x is the value of a pixel in the window, and y is the value of that pixel's neighbor. We then count the number of unique pairs and insert these counts into the matrix in the corresponding row and column where $i = x$ and $j = y$. We finally divide every entry in the matrix by P to normalize the matrix.

From one GLCM, we derive 8 descriptors: the mean, variance, homogeneity, contrast, dissimilarity, entropy, angular second moment, and correlation (Zvoleff, 2020). Note that $p(i, j)$ is the entry in the GLCM at the i^{th} row and the j^{th} column.

K	number of colors to use in GLCM calculation
θ	angle of a given pixel's neighbor
W	odd length of a square sliding window
M	possible number of windows and number of GLCMs for an image
P	$= W^2$, number of pixels and number of pixel pairs in a window
i, j	row, column index for a GLCM
x, y	color value of a pixel, color value of its neighbor
$p(i, j)$	i^{th}, j^{th} entry in the GLCM

Table 1: Variables for GLCM calculation.

1. Mean:

$$f_1 = \mu = \frac{\mu_x + \mu_y}{2}$$

$$\mu_x = \frac{1}{K} \sum_{i=1}^K i \sum_{j=1}^K p(i, j) \quad \mu_y = \frac{1}{K} \sum_{j=1}^K j \sum_{i=1}^K p(i, j)$$

2. Variance:

$$f_2 = \sigma^2 = \sum_{i=1}^K \sum_{j=1}^K (i - \mu)^2 p(i, j)$$

3. Homogeneity:

$$f_3 = \sum_{i=1}^K \sum_{j=1}^K \frac{p(i,j)}{1 + (i - j)^2}$$

4. Contrast:

$$f_4 = \sum_{i=1}^K \sum_{j=1}^K (i - j)^2 p(i,j)$$

5. Dissimilarity:

$$f_5 = \sum_{i=1}^K \sum_{j=1}^K |i - j| p(i,j)$$

6. Entropy:

$$f_6 = - \sum_{i=1}^K \sum_{j=1}^K p(i,j) \log(p(i,j))$$

7. Angular second moment:

$$f_7 = \sum_{i=1}^K \sum_{j=1}^K (p(i,j))^2$$

8. Correlation:

$$f_8 = \sum_{i=1}^K \sum_{j=1}^K \frac{(i - m_x)(j - m_y)p(i,j)}{\sigma_x \sigma_y}$$

$$m_x = \sum_{i=1}^K i \sum_{j=1}^K p(i,j) \quad \sigma_x^2 = \sum_{i=1}^K (i - m_x)^2 \sum_{j=1}^K p(i,j)$$

$$m_y = \sum_{j=1}^K j \sum_{i=1}^K p(i,j) \quad \sigma_y^2 = \sum_{j=1}^K (j - m_y)^2 \sum_{i=1}^K p(i,j)$$

With M possible sliding windows and M possible GLCMs for one image, the 8 descriptors are sort of images themselves: an image with M pixels. To describe the distribution of the texture descriptors in the image, I calculated the mean, standard deviation, skewness, and kurtosis of these 8 descriptors, leading to 32 GLCM-based features per image.

I completed this process for $\theta = -45^\circ$ and 5 different window sizes, $W = 3, 5, 7, 11, 15, 23, 31, 47$, and 63. With each window size giving 32 features, there are $9 * 32 = 288$ GLCM-based features in total.

2.5 Classification

For each image, we have features and a label. With 36 color features and 288 texture features, we have a vector of $F = 36 + 288 = 324$ dimensions to represent each radar image. Also, for each radar image, we have a label of yes or no for the presence of near-surface ice at the center of the image based on the output of the model from Piqueux et al. (2019).

The objective of machine learning is to use an algorithm to learn, understand, and model the relationship between the feature vector and the feature vector's label. Then, the model can predict the label from a new, unseen feature vector. Researchers have developed many different machine learning algorithms and some perform better than others depending on the nature of the data.

Creating a machine learning model is simply a matter of plugging in a training set (the feature vectors and their respective labels) and evaluating it with a testing set (the feature vectors without their labels). I explained the radar image processing and feature extraction in detail because it is unique to this study, but I refrain from going into detail about the technical aspects of the algorithms.

I used random forest (Breiman, 2001) on the entire dataset of 23,650 images with $N = 500$ number of trees built from bootstrapped samples and $K = \sqrt{F} = 18$ number of features tried at each split of the decision tree (Liaw & Wiener, 2002).

3 Results

Random forest gives an internal error estimate similar to an error estimate from cross-validation and can provide which images it correctly classified and misclassified. The random forest out-of-bag estimate of error is 12.29%, meaning the model's approximate accuracy is 87.71%.

	Predict: no ice	Predict: yes ice	Total	Error	Accuracy
Actual: no ice	12903	1380	14283	9.66%	90.34%
Actual: yes ice	1527	7840	9367	16.30%	83.70%
Total	14430	9220	23650	12.29%	87.71%

Table 2: Random forest out-of-bag confusion matrix.

4 Discussion

Classification accuracy of 87% suggests some relationship between the texture of the SHARAD radar image of Mars and the presence of near-surface ice. Machine learning can differentiate between images that have and don't have ice with decent accuracy, purely from image features. Successfully quantifying and interpreting the ground-penetrating radar's speckle-like interference (the background noise in the image) to detect aspects of the subsurface is unheard of and could have huge implications for the interpretation of ground-penetrating radar.

There are more false negatives (where there is ice but the model predicts no ice) than false positives (where there is no ice but the model predicts ice). False negatives mean ice is not causing a noticeable change in texture at certain locations. These false negatives seem to occur most prominently at the lower left part of the map, at around coordinates {longitude: 100, latitude: -50}, where the ice is at a medium depth. Different depths could create different radar reflections

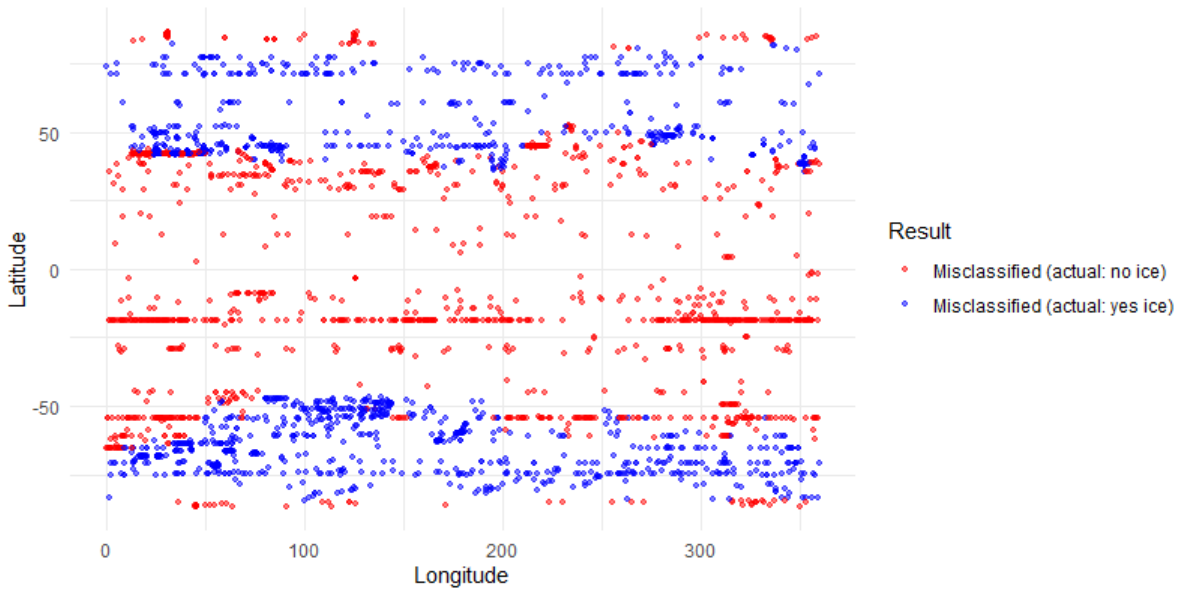


Figure 6: Locations of misclassified radar images on Mars.

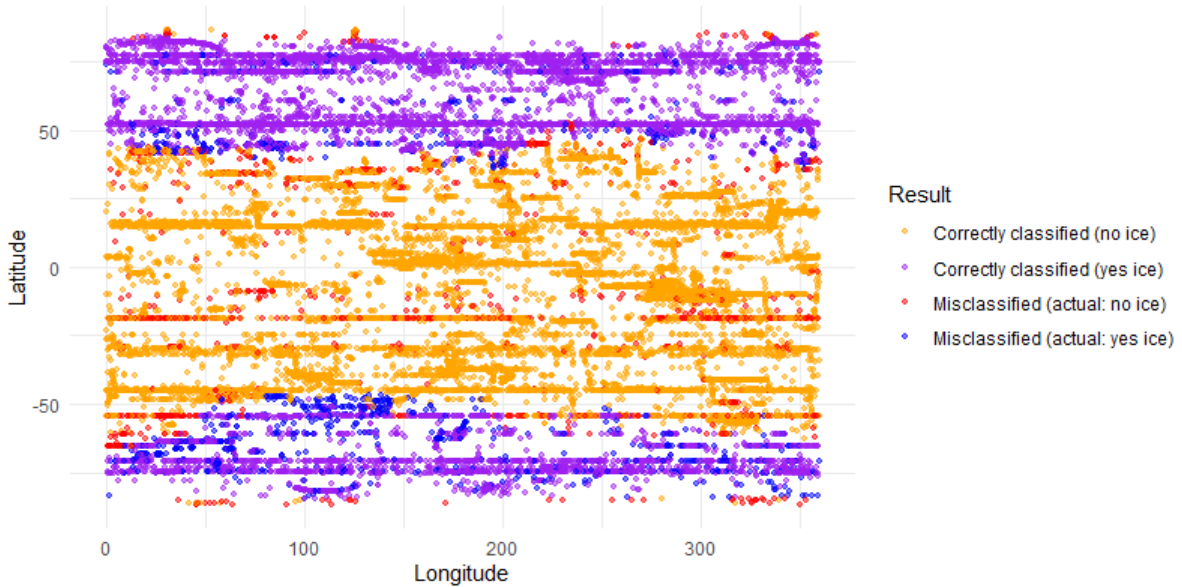


Figure 7: Locations of correctly classified and misclassified radar images on Mars.

and textures and maybe causing some inaccuracy since the model does not account for depth.

There is also a straight line of false positives at around {latitude: -23}. False positives mean areas with no ice are causing a change in texture that makes it look like there is ice. It's unclear why this specific latitude has a lot of misclassified images. It could be that there are just so many radar images at this latitude but with the same overall error rate, creating a large number of misclassifications.

Other misclassified radar images do not seem to follow any pattern and are scattered evenly around the planet. Another reason for error may be that some of the ice is unstable and can appear or disappear depending on variations in weather and climate. The data is from a period of 13 years, so the date of the radar image could affect whether or not there is ice.

According to random forest's variable importance measure (Breiman, 2001), the color features play a minimal role in classification compared to texture features. This finding is unsurprising because color is neither the focus of this study nor much help in measuring speckle-like interference. Future research can try other image features and classification methods to improve prediction accuracy.

The biggest limitation of this study is that it's impossible to know for certain whether the speckle-like interference is causing the relationship between texture and ice. Further research could develop the mathematics that describes the physical properties behind the results or try similar methods with different data, like raw radar data instead of processed radar images. This study's model is not directly applicable to other radar images, like those from MARSIS or other ground-penetrating radars, but the methods are the same, and future research can apply similar techniques to other radars to find near-surface ice.

5 Conclusion

Near-surface ice influences the ground-penetrating radar returns through speckle-like interference. Texture features can quantify the speckle-like interference because it is present in processed radar images, and machine learning can use texture features to distinguish whether there is near-surface ice or not at the location of the image. The ability to measure speckle-like interference opens up many new opportunities to how we use ground-penetrating radar to study Mars and other celestial bodies in continuing humanity's never-ending quest to live among the stars.

References

- Barlow, N. (2008). *Mars: An Introduction to its Interior, Surface and Atmosphere*. Cambridge University Press. <https://doi.org/10.1017/CBO9780511536069>
- Beaty, D. W., Hays, L. E., Davis, R., Bussey, B., Abbud-Madrid, A., Boucher, D., Gertsch, L., Kleinhenz, J., Mueller, R., van Susante, P., Whetsel, C., Zbinden, E., Zurek, R., & Hoffman, S. J. (2016). The Possible Strategic Significance of Mid-Latitude Ice Deposits to a Potential Future Human Mission to Mars [Provided by the SAO/NASA Astrophysics Data System], In *Sixth International Conference on Mars Polar Science and Exploration*. Provided by the SAO/NASA Astrophysics Data System. <https://ui.adsabs.harvard.edu/abs/2016LPICo1926.6059B>
- Boynton, W. V., Feldman, W. C., Squyres, S. W., Prettyman, T. H., Brückner, J., Evans, L. G., Reedy, R. C., Starr, R., Arnold, J. R., Drake, D. M., Englert, P. A. J., Metzger, A. E., Mitrofanov, I., Trombka, J. I., d'Uston, C., Wänke, H., Gasnault, O., Hamara, D. K., Janes, D. M., ... Shinohara, C. (2002). Distribution of Hydrogen in the Near Surface of Mars: Evidence for Subsurface Ice Deposits. *Science*, 297(5578), 81–85. <https://doi.org/10.1126/science.1073722>
- Breiman, L. (2001). Random Forests. *Machine learning*, 45(1), 5–32. <https://doi.org/10.1023/A:1010933404324>
- Campbell, B., & Phillips, R. (2014). *Mars Reconnaissance Orbiter Shallow Radar Radargram Data* [MRO-M-SHARAD-5-RADARGRAM-V1.0]. MRO-M-SHARAD-5-RADARGRAM-V1.0. NASA Planetary Data System. <https://pds-geosciences.wustl.edu/mro/mro-m-sharad-5-radargram-v1/>

- Dundas, C. M., Byrne, S., McEwen, A. S., Mellon, M. T., Kennedy, M. R., Daubar, I. J., & Saper, L. (2014). HiRISE observations of new impact craters exposing Martian ground ice. *Journal of Geophysical Research: Planets*, 119(1), 109–127. <https://doi.org/10.1002/2013JE004482>
- Haralick, R. M., Shanmugam, K., & Dinstein, I. (1973). Textural Features for Image Classification. *IEEE Transactions on Systems, Man, and Cybernetics*, 3(6), 610–621. <https://doi.org/10.1109/TSMC.1973.4309314>
- Liaw, A., & Wiener, M. (2002). Classification and Regression by randomForest. *R News*, 2(3), 18–22. <https://CRAN.R-project.org/doc/Rnews/>
- Long, F., Zhang, H., & Feng, D. D. (2003). Fundamentals of Content-Based Image Retrieval, In *Multimedia Information Retrieval and Management*. Springer. https://doi.org/10.1007/978-3-662-05300-3_1
- Mellon, M. T., Arvidson, R. E., Sizemore, H. G., Searls, M. L., Blaney, D. L., Cull, S., Hecht, M. H., Heet, T. L., Keller, H. U., Lemmon, M. T., Markiewicz, W. J., Ming, D. W., Morris, R. V., Pike, W. T., & Zent, A. P. (2009). Ground ice at the Phoenix Landing site: Stability state and origin. *Journal of Geophysical Research: Planets*, 114(E1). <https://doi.org/10.1029/2009JE003417>
- Orosei, R., Lauro, S. E., Pettinelli, E., Cicchetti, A., Coradini, M., Cosciotti, B., Di Paolo, F., Flamini, E., Mattei, E., Pajola, M., Soldovieri, F., Cartacci, M., Cassenti, F., Frigeri, A., Giuppi, S., Martufi, R., Masdea, A., Mitri, G., Nenna, C., ... Seu, R. (2018). Radar evidence of subglacial liquid water on Mars. *Science*, 361(6401), 490–493. <https://doi.org/10.1126/science.aar7268>
- Picardi, G., Plaut, J. J., Biccari, D., Bombaci, O., Calabrese, D., Cartacci, M., Cicchetti, A., Clifford, S. M., Edenhofer, P., Farrell, W. M., Federico, C., Frigeri, A., Gurnett, D. A., Hagfors,

- T., Heggy, E., Herique, A., Huff, R. L., Ivanov, A. B., Johnson, W. T. K., ... Zampolini, E. (2005). Radar Soundings of the Subsurface of Mars. *Science*, 310(5756), 1925–1928. <https://doi.org/10.1126/science.1122165>
- Piqueux, S., Buz, J., Edwards, C. S., Bandfield, J. L., Kleinböhl, A., Kass, D. M., Hayne, P. O., MCS, & Teams, T. (2019). Widespread Shallow Water Ice on Mars at High Latitudes and Midlatitudes. *Geophysical Research Letters*, 46(24), 14290–14298. <https://doi.org/10.1029/2019GL083947>
- Plaut, J. J., Picardi, G., Cicchetti, A., Clifford, S., Edenhofer, P., Farrell, W., Federico, C., Frigeri, A., Heggy, E., Herique, A., Ivanov, A., Jordan, R., Kofman, W., Leuschen, C., Milkovich, S., Mouginot, J., Nielsen, E., Orosei, R., & Pettinelli, E. (2006). MARSIS Subsurface Sounding Observations of the South Polar Region of Mars [Provided by the SAO/NASA Astrophysics Data System], In *Fourth international conference on mars polar science and exploration*. Provided by the SAO/NASA Astrophysics Data System. <https://ui.adsabs.harvard.edu/abs/2006LPICo1323.8100P>
- Plaut, J. J., Safaeinili, A., Holt, J. W., Phillips, R. J., Head, J. W., Seu, R., Putzig, N. E., & Frigeri, A. (2009). Radar evidence for ice in lobate debris aprons in the mid-northern latitudes of Mars. *Geophysical Research Letters*, 36(2). <https://doi.org/10.1029/2008GL036379>
- Putzig, N. E., Phillips, R. J., Campbell, B. A., Mellon, M. T., Holt, J. W., & Brothers, T. C. (2014). SHARAD soundings and surface roughness at past, present, and proposed landing sites on Mars: Reflections at Phoenix may be attributable to deep ground ice. *Journal of Geophysical Research: Planets*, 119(8), 1936–1949. <https://doi.org/10.1002/2014JE004646>
- Seu, R., Phillips, R. J., Biccari, D., Orosei, R., Masdea, A., Picardi, G., Safaeinili, A., Campbell, B. A., Plaut, J. J., Marinangeli, L., Smrekar, S. E., & Nunes, D. C. (2007). SHARAD

sounding radar on the Mars Reconnaissance Orbiter. *Journal of Geophysical Research: Planets*, 112(E5). <https://doi.org/10.1029/2006JE002745>

Swain, M. J., & Ballard, D. H. (1991). Color Indexing. *International Journal of Computer Vision*, 7(1), 11–32. <https://doi.org/10.1007/BF00130487>

Zhang, D., Islam, M. M., & Lu, G. (2012). A review on automatic image annotation techniques. *Pattern Recognition*, 45(1), 346–362. <https://doi.org/10.1016/j.patcog.2011.05.013>

Zvoleff, A. (2020). *glcm: Calculate Textures from Grey-Level Co-Occurrence Matrices (GLCMs)* [R package version 1.6.5]. R package version 1.6.5. <https://CRAN.R-project.org/package=glcm>